J Mater Sci: Mater Electron **(2023) 34:1891**

Effects of p-type-metal-doping (Ba, Cs, and Y) of the compact-TiO_2 electron transporting layer on the photovoltaic properties of n-i-p perovskite solar cells

U. Nwankwo[1,2,3,4], Agnes C. Nkele[1], Christopher J. Arendse[5], Kenneth I. Ozoemena[6], A. B. C. Ekwealor[1], Rajan Jose[7], Malik Maaza[3,4], and Fabian I. Ezema[1,3,4,*]

[1] *Department of Physics and Astronomy, University of Nigeria, Nsukka, Enugu State, Nigeria*
[2] *Department of Physics, Alex Ekwueme Federal University Ndufu-Alike, Abakaliki, Ebonyi State, Nigeria*
[3] *Nanosciences African Network (NANOAFNET), iThemba LABS-National Research Foundation, 1 Old Faure Road, P.O.Box 722, Somerset West 7129, Western Cape, South Africa*
[4] *UNESCO-UNISA Africa Chair in Nanosciences/Nanotechnology, College of Graduate Studies, University of South Africa (UNISA), Muckleneuk Ridge, P.O. Box 392, Pretoria, South Africa*
[5] *Department of Physics, University of the Western Cape, Private Bag X17, Bellville 7535, South Africa*
[6] *Molecular Sciences Institute, School of Chemistry, University of the Witwatersrand, P O Wits, Private Bag 3, Johannesburg 2050, South Africa*
[7] *Nanostructured Renewable Energy Materials Laboratory, Faculty of Industrial Sciences and Technology, Universiti Malaysia Pahang, 26300 Kuantan, Pahang, Malaysia*

Received: 24 April 2023
Accepted: 21 September 2023
Published online: 29 September 2023

ABSTRACT

Tailoring of charge transport properties of the electron transport layer (ETL) in solution-processible solar cells is continuously addressed not only for the performance enhancements in perovskite solar cells but also in various other applications in nanotechnology. In this work, three p-type dopants: barium, cesium (Cs), and yttrium (Y) with varying crystal radii and charges are doped in the titanium dioxide (TiO_2) material so as to modify the electrical and optical properties of the ETL. The pure and doped TiO_2 films were prepared by spin-coating a sol–gel precursor and their effects on the crystal structure, morphology, optical, electrical and photovoltaic properties of the perovskite solar cells were studied and reported. Among them, Y-doped TiO_2 with similar crystal radii as that of the host titanium atom showed an enhanced photo-conversion efficiency mainly contributed by enhanced open circuit voltage and fill factor. The power conversion efficiency (PCE) for the perovskite absorber layer on Cs- and Y-doped TiO_2 show the maximum PCE of 2.81 and 4.50% respectively. These are encouraging results for optimizing the yttrium doping level and fabrication conditions to further push the performance indicators of PSCs.

Address correspondence to E-mail: Fabian.ezema@unn.edu.ng

https://doi.org/10.1007/s10854-023-11373-y

1 Introduction

Organic-inorganic metal halides (Organometal) based perovskite solar cells (PSCs) have received great attention due to their process-ability from solutions, low cost, and ability to be grown on flexible substrates [1, 2]. The phenomenal increase in the power conversion efficiency (PCE) of PSCs from 3.8% (in 2009) to 26% (in 2022), has drawn more attention from researchers in this area [3–5]. Ever since the first report on the photovoltaic effect in the PSCs, many organometal perovskite materials have emerged in response to a continuous effort to improve performance [6]. The most frequently used active absorber perovskite for PSCs is methyl ammonium lead iodide ($MAPbI_3$), and this is due to their properties such as direct bandgap transition, high absorption coefficient, broad absorption spectrum in the visible region, weak exciton (electron-hole pair) binding energy, long carrier diffusion length, and low intrinsic defects [7–9]. In recent years, various methods, both in air and under vacuum processing conditions, used to fabricate the perovskite absorber layer have been reported [9, 10]. Spin-coating, dip-coating, chemical vapor deposition, or a combination of the two methods have been used to fabricate an optimized pinhole-free perovskite absorber layer [11, 12]. The solution-based processing by spin-coating and dipping-coating has shown to be the most affordable and the easiest method to make perovskite absorber layers in small and large areas. However, the photovoltaic performance of the PSC depends on the method of deposition and growth condition used [13, 14]. The spin-coating and dip-coating parameters such as spin-time, spin-speed, and dip-time as well as the annealing temperature play a major role in the outcome of the PSC devices. In addition, the concentration of the lead iodide (PbI_2) and methyl ammonium iodide (MAI) dissolved in a solvent also determines the physical and chemical properties of the $MAPbI_3$ [15]. PSCs are divided into three major components, and they include the electron transporting layer (ETL), the active absorber layer, and the hole transporting layer (HTL). The three fundamental processes of the PSCs are the generation of electron-hole pair in the active absorber layer, the separation of electron and hole, and the collection of electron and hole [16]. The photo-generated charge carriers are required to be extracted through the transporting layers to avoid recombination or accumulation in the interfaces between the active layer and transporting layers [17, 18]. Efficient ETL and HTL are those that prevent the photo-generated charge carriers from recombining or piling at the interfaces between the layers before transporting them to the ETL and HTL.

The ETL is an important component of the PSC in all device architecture such as in the planar and mesoporous structures [19]. Numerous metal oxides and methods have been used to fabricate the ETL of the planar or mesoporous structure PSCs. Currently, TiO_2 has proven to be the most stable and effective ETL used aside from zinc oxide (ZnO) and tin oxide (SnO) for the extraction of electrons in PSC [20]. To achieve a stable and efficient TiO_2 ETL, the method of deposition plays a vital role. Several methods such as wet chemical, SILAR-induced gel method, doctor-blade, spin-coating, ion-beam evaporation, sputtering, and atomic layer deposition have been reported [21, 22]. The spin-coating method is the most widely used for the fabrication of TiO_2 ETL in the PSC due to its less complexity, cheaper, and fewer energy requirements. Despite the desirable properties possessed by TiO_2, the material suffers from low conductivity due to the oxygen vacancies at the lattice site. Moreover, the energy level offset show that the conduction band of the TiO_2 is lower than the conduction band of the perovskite absorber layer, causing less flow of electrons from the perovskite layer [23–25]. To address these issues of low conductivity and band offset to improve the electron extraction, doping is required to modify the vacancies at the lattice site and fermi-level [24, 26]. The electron extractions have been improved by doping TiO_2 with niobium (Nb-doped TiO_2), zinc (Zn-doped TiO_2), magnesium (Mg-doped TiO_2), and aluminum (Al-doped TiO_2), etc., but more studies are needed to further improve them [1, 24, 27–30]. An increase in the open-circuit (V_{oc}) and short-circuit current density (J_{sc}) has been observed by suitably doping TiO_2 with transition metals in many soar cell configurations in which they form an ETL [31–33].

In this study, we synthesized pure, Ba, Cs and Y doped c-TiO_2 layer as an effective electron extraction layer by sol-gel combined spin-coating deposition on a patterned fluorine doped tin oxide (FTO) substrate. The three dopants (Ba^{2+}, Cs^{+}, and Y^{3+}) have valences less than + 4 of the host titanium ion, and they are p-type dopants to TiO_2 which is an n-type semiconductor. The p-type doping in TiO_2 reduce oxygen concentration which improves the electrical conductivity of the resulting material. The perovskite active layers were deposited on this optimized doped c-TiO_2 by

two-step spin-coating sequential deposition. The electron transporting, perovskite absorber, and hole transporting layers were all fabricated by the spin-coating method, which further encourages the reduction in the cost of the PCS. We also studied the structural, surface morphology, electrical and optical properties of the Ba-doped TiO_2, Cs-doped TiO_2, and Y-doped TiO_2 and the perovskite active layer on different doped c-TiO_2. The motivation behind the p-type doping adopted in this work is to reduce the oxygen atom concentration when Ba^{2+}, Cs^{2+}, and Y^{3+} replaces the Ti^{4+} ions in the TiO_2 lattice. Lowering of oxygen atom increases the metallicity and hence the electrical conductivity of the resulting materials [33]. The PCE of the completed PSC devices was studied and discussed. This work is expected to add more understanding to the method of spin-coating for the preparation of perovskite active layer and suitable ETL to be used for efficient PSCs.

2 Experimental details

2.1 Preparation of the compact TiO_2 layers and the fabrication of $MAPbI_3$ perovskite solar cells

The perovskite solar cells were fabricated by a two-step spin-coating process on the c-TiO_2 layer which is deposited on the FTO substrate as shown in Fig. 1. The FTO substrates were etched with Zn powder and 2.0 M of hydrochloric acid (HCL), and then they were cleaned in the following steps: washed in detergent, sonicated in warm deionized water, isopropanol alcohol (IPA) for 30 min, and finally in warm deionized water. The clean etched FTO substrates were dried for 20 min in the air. The titanium precursor solution for the c-TiO_2 was prepared by dissolving 375 µL of titanium isopropoxide (TTIP) in 2500 µL of ethanol (99% alcohol), 35 µL of 2.0 M HCl mixed with 2500 µL ethanol (99.9% alcohol), and then add the acidic-ethanol solution into the titanium solution. The titanium precursor solution was stirred at room temperature for 2.5 h until the transparent solution was obtained. For doped titanium precursor, 54 mg of barium oxide (BaO) for Ba-doped, 60 mg of cesium chloride (CsCl) for Cs-doped, and 80 mg of yttrium (III) oxide (Y_2O_3) for Y-doped TiO_2 was dissolved in 2500 µL ethanol to obtain 0.14 M doping concentration and added into the acidic-titanium ethanol solution under constant stir at room temperature until the solute dissolves completely. The compact layers of pure, Ba-doped, Cs-doped, and Y-doped TiO_2 were deposited by spin-coating the obtained titanium precursor solutions on the cleaned etched FTO substrates at 3000 rpm for 30 s, pre-heated for 10 min, and annealed at 400 °C for 30 min. The PbI_2 precursor solution was prepared by dissolving 390 mg of PbI_2 powder in a mixture of 900 µL dimethylformamide (DMF) and 100 µL dimethylsulfoxide (DMSO), transferred into capped bottles, and then heated at 65 °C for 3 h under constant stirring. 40 µL of the PbI_2 solution at 65 °C was spin-coated on the c-TiO_2/doped-TiO_2 substrates at 7000 rpm for 35 s on a substrate temperature of 40 °C, preheated at 40 °C for 4 min and dried at 105 °C for 5 min to form a yellow layer in the first step, followed by the conversion of the PbI_2 layer to $MAPbI_3$ by spin-coating the solution MAI dissolved

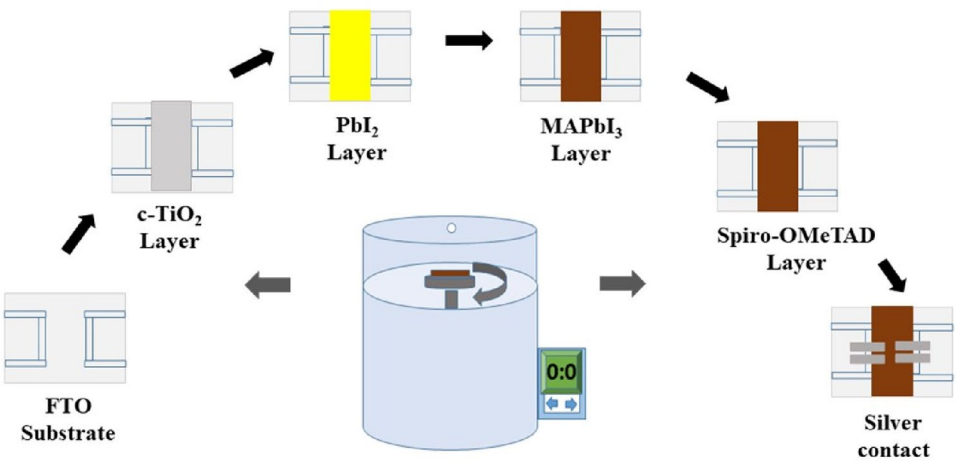

Fig. 1 Experimental steps for the deposition of perovskite solar cell by spin-coating

in IPA. Further details of the completed FTO/c-TiO_2/$MAPbI_3$/spiro-OMeTAD/Ag device can be found in this report [34].

2.2 Characterization of c-TiO_2 and $MAPbI_3$ perovskite absorber layers

The structural information of the synthesized pure, Ba-, Cs- and Y-doped TiO_2, and $MAPbI_3$ layers were obtained by X-ray diffraction technique (XRD, performed with D8-Brucker powder diffractometer with a theta-theta goniometer, and CuK_α radiation $\lambda \sim 0.154$ nm). The optical bandgap and absorbance of the bulk and films were analyzed in Agilent Cary 7000 UV–vis NIR universal measurement spectrophotometer. Carl Zeiss mA 10 model field-emission scanning electron microscope was used to study the surface morphology, average grain size, and chemical composition of the microstructure synthesized. The carrier concentration and mobility of the synthesized c-TiO_2/doped TiO_2 layers were studied using the ECOPIA hall effect measurement system (HMS-3000 VER 3.5). Solar cell parameters were obtained by the *J–V* characteristics measurement under irradiation of 100 mW/cm^2 AM 1.5 standard simulated sunlight at room temperature by Keithley 2420 source meter. The shadow mask used for the solar testing and the active area of the solar cells was 0.0512 cm^2. These characterizations were carried out at iThemba-LABS, National Research Foundation and University of Western Cape, South Africa.

3 Results and discussion

3.1 Structural, surface morphology, and optical properties of pure/doped TiO_2

The XRD patterns of the dried titanium precursor annealed at 500 °C for 30 min for (a) pure, (b) Ba-, (c) Cs- and (d) Y-doped TiO_2 exhibit the anatase phase of TiO_2 as shown in Fig. 2. The observed XRD pattern was all crystalline, with the anatase main peak appearing at the 2theta value of 25.45°, 25.33°, 25.28°, and 25.30° corresponding to the (101) crystal plane of the anatase phase of pure, Ba-, Cs- and Y-doped TiO_2. There is no peak from the other phases of TiO_2. The indexed diffraction peaks of the four doped-TiO_2 correspond to the body-centered tetragonal structure, with unit cell

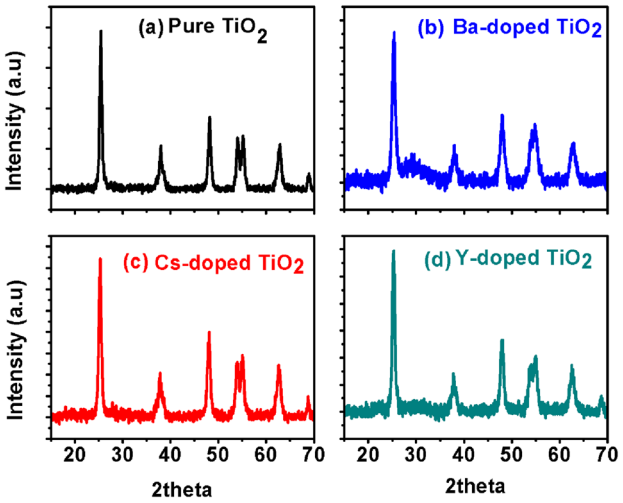

Fig. 2 X-ray diffraction patterns of **a** Pure, **b** Ba-doped, **c** Cs-doped and **d** Y-doped TiO_2

lattice parameters of $a = b = 3.79$ Å, $c = 9.51$ Å (PDF #: 00-021-1272).

The estimated lattice parameters are ($a = b = 3.77$ Å, $c = 9.29$ Å), ($a = b = 3.78$ Å, $c = 9.41$ Å), ($a = b = 3.78$ Å, $c = 9.51$ Å) and ($a = b = 3.79$ Å, $c = 9.44$ Å) for the pure, Ba-, Cs-, Y-doped TiO_2 respectively. The average crystallite size (D) of the synthesized pure and doped TiO_2 nanoparticles were estimated using Scherrer equation as shown in Eq. (1) [35, 36];

$$D = \frac{K\lambda}{\beta\cos\theta} \tag{1}$$

where K is the Scherrer constant, λ is the wavelength of the X-ray source (0.154 nm), β is the full width at half maximum (FWHM) and θ is the Bragg diffraction angle. The D of pure and doped TiO_2 nanoparticles as well as their lattice parameters are summarized in Table 1. As the K was assumed, the calculated D values are estimates. In this paper, $K = 0.94$ was used, considering that the present crystals are spherical as shown in Fig. 3. The crystallite sizes of the nanoparticles decrease when the dopant was added to the host titanium precursor, and there is a significant change in the size when doped with Ba. However, the three metal dopants which are a p-type, generate oxygen deficiency in the p-orbitals thereby uplifting the fermi-level to improve the electrical conductivity. This conductivity depends on the grain size, surface morphology, chemical properties, and doping [33]. The ionic radii of Ba^{2+}, Cs^{+}, Y^{3+}, and Ti^{+4} are 0.135 nm, 0.175 nm,

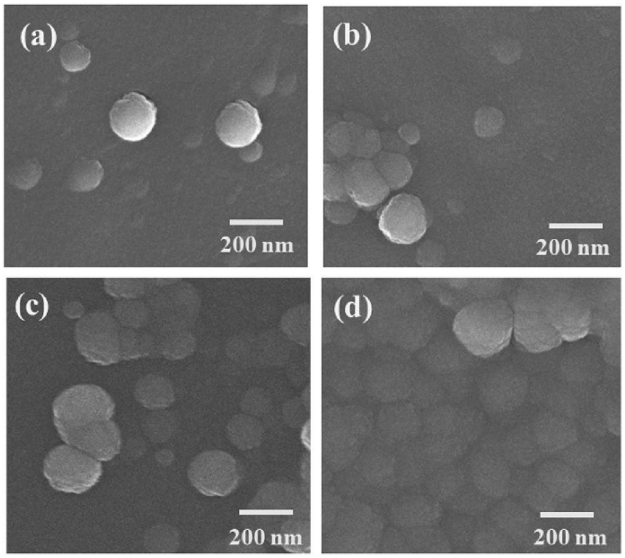

Fig. 3 SEM image for **a** Pure, **b** Ba-doped, **c** Cs-doped and **d** Y-doped TiO_2

0.101 nm, and 0.088 nm respectively. The shift in the c-axis of the lattice parameter is correlated with the ionic radii of the dopant. The Cs dopant with the largest ionic radius possesses the largest size in the c-axis of the lattice parameters, and vice versa to pure TiO_2 without doping. The nanoparticles are spherical-like in shape as shown in Fig. 3.

The surface morphological visual study in Fig. 3 reveals that the nanoparticles of the pure and doped TiO_2 are spherical, and there is cluster observation in the Ba-, Cs-, and Y-doped TiO_2. The cluster could be a result of the dopant added during synthesis. The SEM images of (b), (c), and (d) showed that more nanoparticles are grown in the doped TiO_2 than the pure TiO_2. Figure S1 shows that the estimated grain size for pure, Ba-, Cs-, and Y-doped TiO_2 are 58.13 nm, 46.93 nm, 46.24, and 56.86 nm respectively. The cluster of the nanoparticles in the doped TiO_2 can affect the electron extraction from the perovskite absorber layer, and the performance of the perovskite solar cell can be improved [30, 33, 37]. However, the energy-dispersive X-ray spectrum reveals the dopants are present in the materials except for Ba-doped which shows no dopant present in Fig. S2.

Figure 4 shows the optical bandgap energy for indirect band transition obtained by the Tauc relation in Eq. (2);

$$(\alpha h\nu)^{1/n} = \mathrm{B}\left(h\nu - E_g\right) \tag{2}$$

α is the coefficient of absorption, $h\nu$ is the photon energy, Eg is the optical bandgap, B is the factor dependent on the transition, and n is the power-dependent of the optical absorption. [38]

The estimated optical bandgap energy for pure-TiO_2, Ba-doped, Cs-doped, and Y-doped TiO_2 are 3.52 eV, 3.44 eV, 3.50 eV, and 3.48 eV respectively as shown in Fig. 4. The bandgap of pure TiO_2 show the highest among them, and Ba-doped TiO_2 possesses the lowest bandgap energy. The bandgap energies of the pure and doped TiO_2 show an increase of 0.24–0.32 eV more than the optical bandgap of pure and doped TiO_2 synthesized by other methods as reported in the literature [19, 21]. The lowering of the optical bandgaps on doped-TiO_2 could be attributed to the shift in the conduction band and valence band of the parent material. The Ba- and Y-doped TiO_2 show a lowering in the optical bandgap, which can be understood from the shifting of the valence band and conduction band towards the lower energy orbitals and the higher energy orbitals respectively. However, the increase in the optical bandgap of Cs-doped TiO_2 than Ba- and Y-doped can be attributed to the shifting of the conduction band shift towards the higher energy orbitals such as the 4d-orbital than the 3d orbitals in Ti [33, 39]. In addition, the bandgap widening and reduction are related to how transparent the c-TiO_2 layer appears visually. The doped Ba- and Cs-doped TiO_2 appeared dim in color compared to the pure and Y-doped TiO_2. This transparency in pure and Y-TiO_2 layers is related to the optical bandgap widening. No relationship between the crystallite size of the synthesized

Table 1 Summary of the pure, and doped TiO_2 (anatase phase) main peak position, crystallite size, and lattice parameters

Sample	2theta (°)	FWHM (°)	Crystallite size (D) (nm)	lattice parameters (Å)
Pure TiO_2	25.45	0.58	15	$a=b=3.77$, $c=9.29$
Ba-doped TiO_2	25.33	0.82	11	$a=b=3.78$, $c=9.41$
Cs-doped TiO_2	25.28	0.60	14	$a=b=3.78$, $c=9.51$
Y-doped TiO_2	25.30	0.65	13	$a=b=3.79$, $c=9.44$

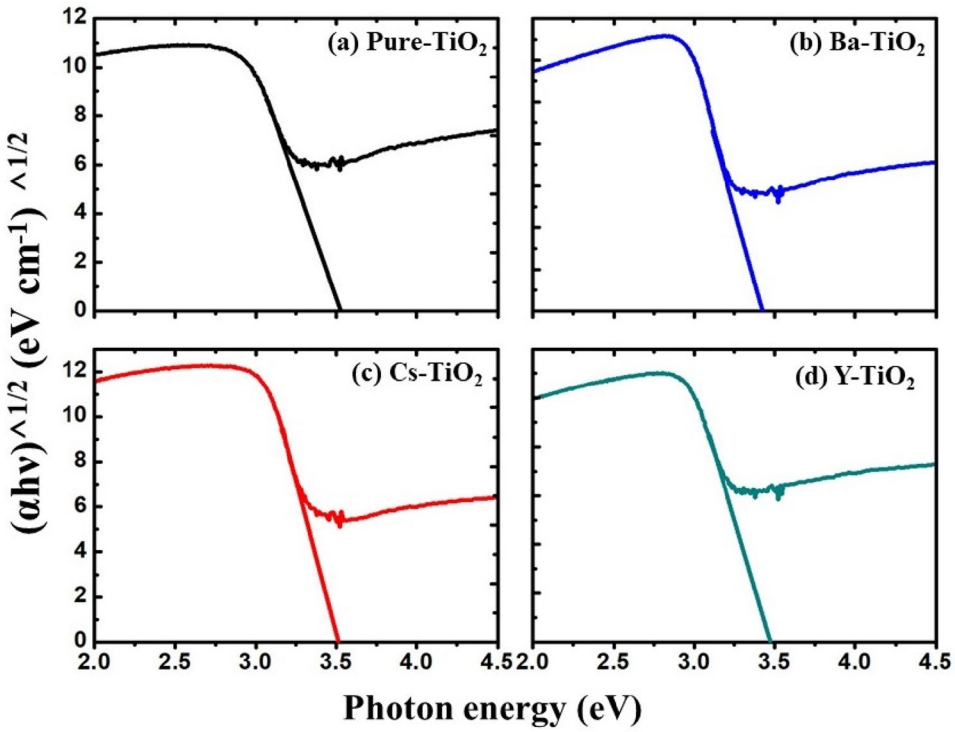

Fig. 4 Tauc plots showing the optical bandgap of **a** pure TiO_2, **b** Ba-doped TiO_2, **c** Cs-doped TiO_2 and **d** Y-doped TiO_2

nanoparticles and the optical bandgap energies was observed. These results suggest that the metal ions effectively doped in TiO_2 and the resulting material is expected to show doping-induced electrical properties when they are used as an ETL in PSCs [27].

The electrical measurement was carried out using the Van der Pauw four-probe contact method to obtain bulk carrier concentration. The pure, Ba-doped Cs-doped, and Y-doped TiO_2 layers measuring thickness ~ 50 nm and area ~ 1.0 cm^2 deposited on glass substrates were the sample for the electrical property measurements. 5.0 nA current was applied to one end of the sample holder and the voltage drops were measured across the other end of the sample by applying 0.550 T perpendicular to the plane of the c-TiO_2 layers. The bulk carrier concentration for the pure, Ba-doped TiO_2, Cs-doped TiO_2, and Y-doped TiO_2 were estimated to be $7.64 \times 10^{12}/cm^3$, $1.09 \times 10^{13}/cm^3$, $2.99 \times 10^{13}/cm^3$, and $2.75 \times 10^{13}/cm^3$ respectively. The carrier concentration for the Ba-TiO_2, Cs-TiO_2, and Y-TiO_2 improved due to the p-type doping in the TiO_2, generating oxygen deficiency that contributes to the improved electrical conduction. This improvement of the electrical conductivity is possible because the three dopants (Ba^{2+}, Cs^+, and Y^{3+}) have valences less than Ti^{4+} of the host titanium ion, and the fermi-level of the host TiO_2 is modified due to lattice strain caused by the dopant. Consequently, the fermi-level shifts towards the conduction band, thereby promoting the movement of electrons to the conduction band. The carrier concentration obtained for the doped c-TiO_2 increases, which is an indication that the doped samples are more conducting than the pure, and electrons from the perovskite active layer can effectively be transported.

3.2 Structural, surface morphology, and optical properties of the $MAPbI_3$ on pure/doped TiO_2

Figure 5 shows the XRD pattern of the spin-coated PbI_2 layer and converted $MAPbI_3$ deposited on the compact pure, Ba-, Cs-, and Y-doped TiO_2 layer. The XRD spectra of the PbI_2 and perovskite absorber layer deposited of pure, Ba, Cs, and Y-doped TiO_2 are all the same for the four c-TiO_2 layers. Figure 5a shows the X-ray diffraction pattern of the PbI_2 layer which was first deposited on the c-TiO_2 before conversion. PbI_2 layer XRD spectra show all the major peaks from PbI_2, with the main peak appearing at the 2theta position of 12.70° corresponding to the (001) crystal plane, indexed to be a hexagonal crystal structure. Figure 5b shows the converted $MAPbI_3$, which is the second deposition by spin-coating. Aside from the remnant

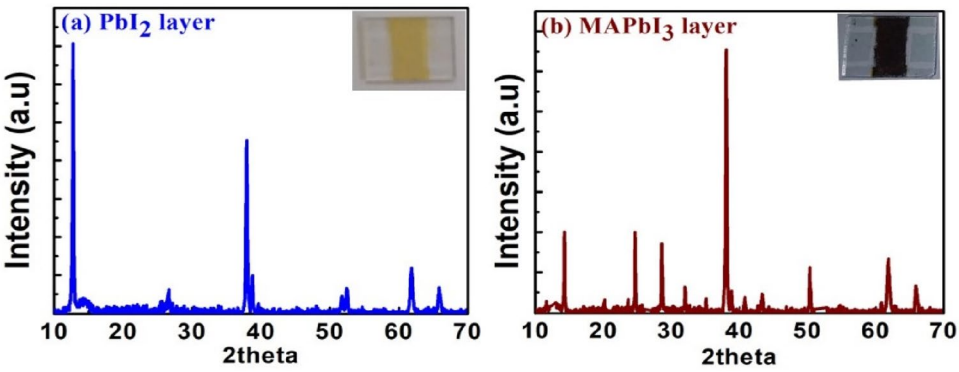

Fig. 5 X-ray diffraction pattern of **a** PbI_2 layer, **b** $MAPbI_3$ layer

PbI_2 peak at 12.70° observed in the $MAPbI_3$ X-ray diffraction pattern, the sets of peaks that emerge on conversion PbI_2 into $MAPbI_3$ layer are 13.80°, 14.20°, 19.95°, 28.79°, 31.88°, 40.72°, and 43.15° corresponding to the reflection from (002), (110), (112), (004), (213), (224), and (314) planes.

These observed X-ray diffraction patterns of $MAPbI_3$ are consistent with the XRD pattern of the $MAPbI_3$ reported in the literature [4, 36]. The crystal structure of the $MAPbI_3$ layer is related to the tetragonal perovskite structure. There is no unknown peak observed in the X-ray diffraction of the PbI_2 and $MAPbI_3$ layer and no phase of perovskite structure was observed. Figure 5b shows that the conversion from PbI_2 to $MAPbI_3$ was complete. However, the XRD patterns of the PbI_2 and $MAPbI_3$ layers are accompanied by the main peak of the FTO substrate. The calculated average crystallite size of the PbI_2 and $MAPbI_3$ are 42 and 81 nm respectively. The average crystallite size of $MAPbI_3$ was found to be larger than the size of PbI_2.

Figure 6a–d shows the SEM image of the $MAPbI_3$ deposited on the Pure, Ba-doped, Cs-doped, and Y-doped TiO_2. The morphology of the $MAPbI_3$ on the pure TiO_2 nanostructure shows a combination of nanosphere and nanorods, with little particle cluster present in the SEM image. The nanostructure of the $MAPbI_3$ on the Ba-doped TiO_2 is nanosphere and nanorod-like shape particles. The SEM image of pure TiO_2 and Ba-doped TiO_2 shows an irregular shape of particles. The nanosphere-like shape of the particles observed for $MAPbI_3$ grown on Cs-doped and Y-doped TiO_2 is an indication of well-formed and regular nanoparticles. The photo-generated charge carriers are expected to be generated in these absorber layers. The cross-sectional SEM micrograph of the layers of FTO substrate, TiO_2, $MAPbI_3$, and Spiro-OMeTAD are shown in Fig. 6e. The interfacial overlap of layers was not observed in the cross-sectional SEM image and there is no interfacial diffusion of layers in the perovskite solar cell. The visual thickness of the $MAPbI_3$ layer on the SEM image is larger than the thickness of the ETL (TiO_2) and HTL (Spiro-OMeTAD). The perovskite solar cell was designed in such a way that the thickness of ETL and HTL is thinner than the absorber layer, and to allow effective transport of photo-generated charge carriers to the top and bottom electrodes [40, 41].

Figure 7 shows the UV–vis absorption spectra of the $MAPbI_3$ layer on Pure TiO_2 (black), Ba-doped TiO_2 (red), Cs-doped TiO_2 (blue), and Y-doped TiO_2 (green). The absorption intensity shows that the $MAPbI_3$ layer on pure and Cs-doped TiO_2 are the highest, and lower absorbance was observed for $MAPbI_3$ on Ba- and Y-doped TiO_2. The lower absorbance could be related to the ionic radius of ETL, as the ETL with a small ionic radius shows lower absorption. The absorption edges in the $MAPbI_3$ layers of the absorbance spectra are uniform and occur at 755 nm (1.64 eV). However, the optical bandgap estimated from the Tauc plot for the $MAPbI_3$ layer on the different c-TiO_2 for direct band transition is 1.63 eV as shown in Fig. S3. This value is the same for the $MAPbI_3$ layer on Ba-, Cs-, and Y-doped TiO_2. The obtained optical bandgap is consistent with values reported for the Pb-based perovskite absorber layer [10, 42, 43].

3.3 Photovoltaic performance of the perovskite solar cells

The best-performing perovskite solar cells fabricated on different c-TiO_2 layers by spin-coating are presented in this section. Figure 8 shows the *J–V* characteristics of $MAPbI_3$ solar cell on different ETLs. The

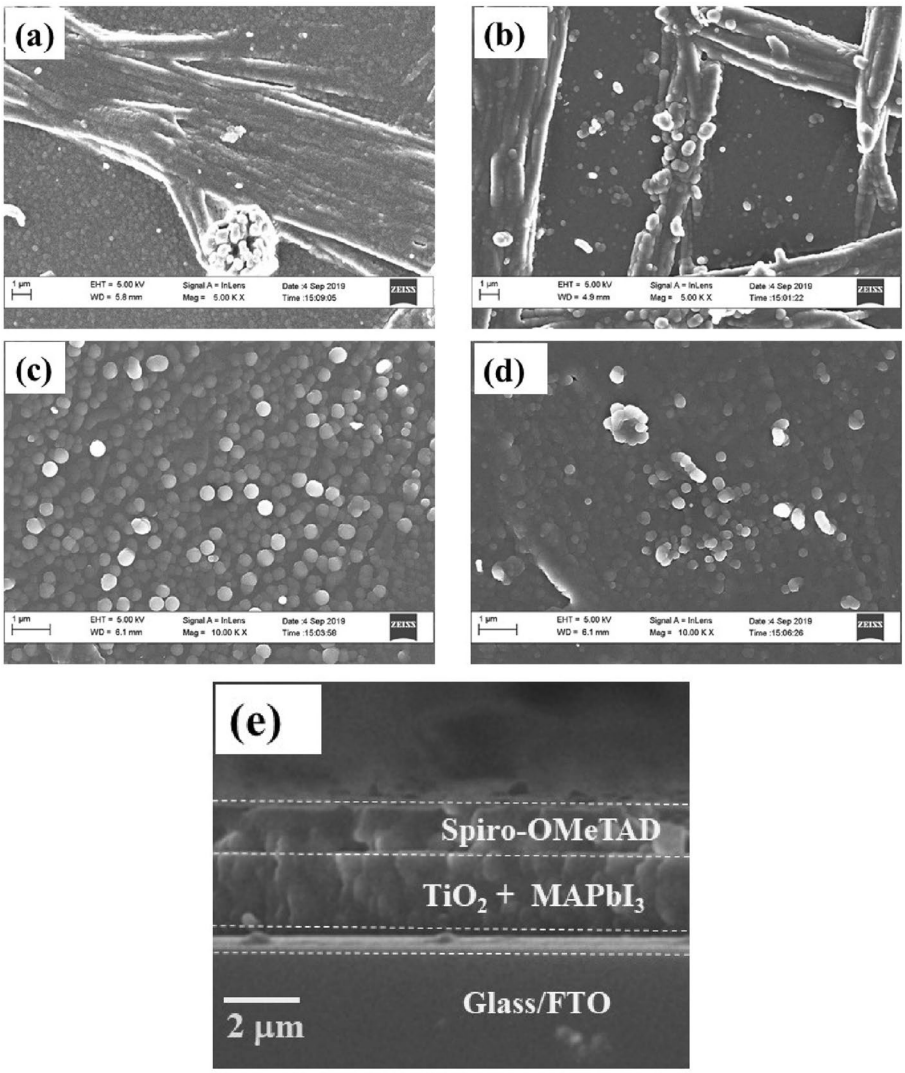

Fig. 6 SEM image of the solution-based $MAPbI_3$ layer on **a** Pure, **b** Ba-doped, **c** Cs-doped, **d** Y-doped TiO_2, **e** Cross-sectional SEM image of $MAPbI_3$ layers by spin-coating

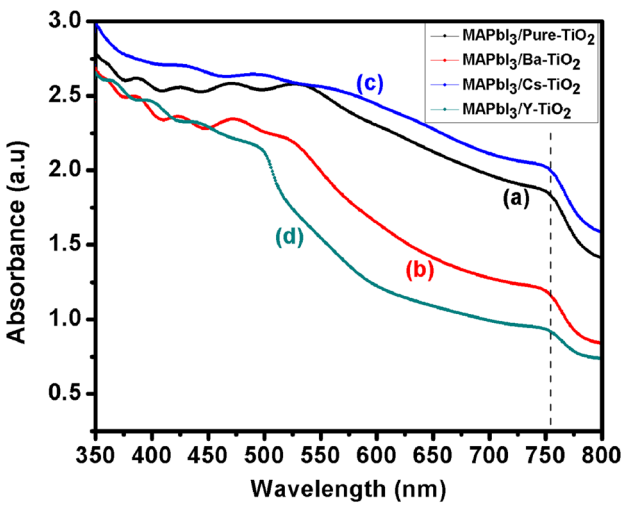

Fig. 7 UV–vis absorption spectra of $MAPbI_3$ layer on **a** Pure TiO_2, **b** Ba-doped TiO_2, **c** Cs-doped TiO_2 and **d** Y-doped TiO_2

perovskite solar cell parameters were obtained from the photocurrent density-voltage curve of the $MAPbI_3$ on pure, Ba-, Cs- and Y-doped c-TiO_2 layers as device (#1, #2), device (#3, #4), (#5, #6) and device (#7, #8) respectively. The current density (J_{sc}), open-circuit voltage (V_{oc}), fill factor (FF) and PCE were obtained from the photocurrent density-voltage curve and are summarized in Table 2. The photovoltaic parameters are influenced by the type of c-TiO_2 layer used for the deposition of the $MAPbI_3$ layer. From Table 2, the $MAPbI_3$ on Y-doped TiO_2 shows the highest *PCE* (3.99%, 4.50%) than that $MAPbI_3$ grown Pure-TiO_2, Ba-doped TiO_2 and Cs-doped TiO_2 layers. The $MAPbI_3$ grown on pure and Ba-doped TiO_2 show the lowest PCE (0.80%, 0.89%). In addition, the J_{sc}, V_{oc}, and FF of the $MAPbI_3$ on Y-doped TiO_2 also show larger values than the other type of c-TiO_2 layers. Device #2 and

Table 2 Photovoltaic parameters of $MAPbI_3$ grown on Pure TiO_2, Ba-TiO_2, Cs-TiO_2 and Y-TiO_2

$MAPbI_3$ on c-TiO_2	Device	*Jsc* (mA/cm^2)	*Voc* (V)	FF	*PCE* (%)
Pure TiO_2	#1	11.07	0.43	0.27	1.29
	#2	5.78	0.44	0.21	0.80
Ba-doped TiO_2	#3	8.62	0.45	0.23	0.89
	#4	10.23	0.46	0.22	1.03
Cs-doped TiO_2	#5	10.57	0.76	0.35	2.81
	#6	9.05	0.73	0.34	2.25
Y-doped TiO_2	#7	14.82	0.82	0.37	4.50
	#8	12.34	0.77	0.42	3.99

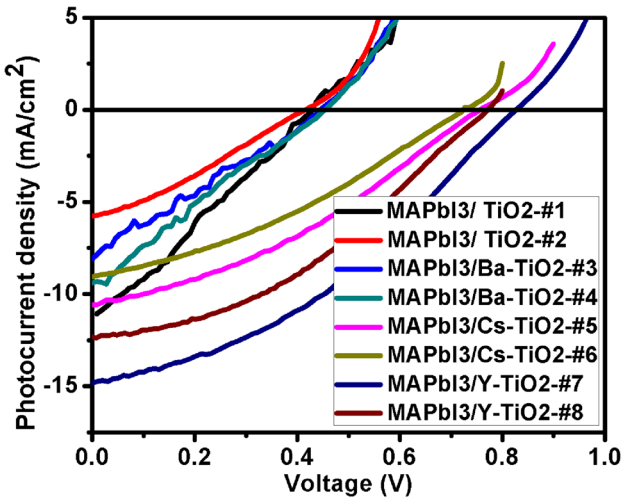

Fig. 8 Photocurrent density-voltage characteristics for devices (#1– #8) $MAPbI_3$ on different c-TiO_2 (pure and doped TiO_2)

device #3 of the perovskite absorber layer grown pure TiO_2 and Ba-doped TiO_2 show the lowest photocurrent density respectively. The V_{oc} of device #2 of the one grown on the Ba-TiO_2 is more than that of device #3 grown on the pure-TiO_2. However, the performance of the current devices is significantly lower than the state-of-the-art PSCs, which is likely to result from the non-ideal fabrication conditions during this work. Nevertheless, one of the primary objectives of this work is to track the relative advantages of the doped TiO_2 in its role as an ETL in PSCs for the un-doped analog. Therefore, within the limitations of fabrication conditions, this primary objective has a positive outcome.

This result indicates that the PCE can be improved by doping TiO_2 ETL with yttrium. The incorporation of metal dopant is vital for the electron transport from the absorber layer, and this was noticed in the values of J_{sc}, V_{oc}, and FF for Cs- and Y-doped TiO_2 layers. The reduction in the FF lower than 50% is due to the contact resistance of the individual device. The improvement in the V_{oc} from 0.43 V for perovskite grown on pure TiO_2 to 0.82 V for perovskite on Y-doped TiO_2 is an indication that there is a modification on the Fermi-level, which could be responsible for the increase in conduction. The increase in conduction also improved the electron extraction from the photo-absorber layer. Moreover, the thickness of the ETL was compact to improve the electron transport, and to avoid recombination of the photo-generated charge carriers in the photo-absorber layer. There is a correlation between the results observed in the photovoltaic parameters and the SEM micrograph of the perovskite absorber layer grown on different c-TiO_2/doped-TiO_2. The SEM micrograph of the perovskite absorber layer grown on the pure TiO_2 and Ba-doped TiO_2 layer shows a clustered nanorod-like particle. This clustered nanorod observed in the SEM image can trigger the recombination of photo-generated charge carriers in the perovskite absorber layer before extraction. The nano spherical-like particle observed in the perovskite absorber layer grown on Cs- and Y-doped TiO_2 shows better photovoltaic parameters as shown in Table 2. This is an indication that for a perovskite solar cell to perform efficiently, the particle shape should be a spherical-like particle. A nanorod perovskite absorber layer formed results in poor photovoltaic performance.

Despite the reduction in the photovoltaic parameters of the overall perovskite solar cells, the p-type doping of the TiO_2 ETL influences the optical and electrical properties of the PSCs. The yttrium-doped TiO_2 is more promising than the other in improving the electronic properties of the ETL, and thereby enhancing the photovoltaic parameters. The PSC grown on Y-doped TiO_2 show an enhanced J_{sc} and V_{oc} when compared with pure, Ba- and Cs-doped TiO_2. The PCE results show that the photovoltaic parameter can be modified better by doping with transition metal ions with 3d orbitals close to oxygen 2p orbital to improve the electron extraction from the photoactive layer. The values of the V_{oc} for perovskite grown on the Cs-doped TiO_2 is an indication of the electronic medication induced by the Cs-ion dopant in the ETL. The Cs- and Y-doped TiO_2 fit properly with the p-type doped model as shown in their optical and electrical properties of the ETL layers while the Ba-doped TiO_2 shows an inconsistent behavior to the former. However, the

method of deposition for both c-TiO_2 and the perovskite absorber layer could also determine the outcome of the photovoltaic parameter.

4 Conclusions

The perovskite solar cells were successfully fabricated by a two-step sequential deposition process using pure and p-type metal (Ba, Cs, and Y) doped TiO_2 as a compact electron transport layer (c-TiO_2) on a pattern FTO substrate. An increase in the c-axis lattice parameter of TiO_2 and lowering of crystallite size confirmed the doping of these metal ions in the parent TiO_2 lattice. The photovoltaic performance of the devices varied with the metal dopant of c-TiO_2 layers. The effect of Ba-, Cs-, and Y-doping on the changes induced by the p-type dopant on the perovskite absorber layers was studied. The average PCE for the perovskite absorber layer on pure, Ba-, Cs-, and Y-doped TiO_2 are 1.69%, 0.96%, 1.92%, and 4.25%, respectively. The PCE for the perovskite absorber layer on Cs- and Y-doped TiO_2 show the maximum PCE of 2.81 and 4.50% respectively, and with an improved J_{sc}, and V_{oc}. However, the SEM image of the perovskite absorber layers with spherical-like shapes shows better performance than those with nanorod-like shapes. These results suggest that the grain formation of the perovskite absorber layer assists in producing high-quality photovoltaics.

Acknowledgements

The authors acknowledge the financial support of AE-FUNAI TETFUND. C.A acknowledges the financial support of the National Research Foundation of South Africa (GUN: 93212). FIE (90407830) graciously acknowledge UNISA for VRSP Fellowship award. We graciously acknowledge the grant by Nigerian Communications Commission under Contract Number NCC/R&D/UNN/014.

Author contributions

UN carried out the experimental work and drafted the manuscript. CJ Arendse and MM provided access for the experimental measurements, and ACN did the SEM analysis. KIO and RJ read the approved submitted manuscript. ABCE and FIE supervised the project. All authors read and approved the final manuscript.

Funding

The authors would like to acknowledge the financial support of the following bodies; Tertiary Education TrustFund (TETFUND) from the Alex Ekwueme Federal University Ndufu-Alike, Ikwo, Nigeria, National Research Foundation of South Africa (GUN: 93212), Vitreo-Retina Society of Philippines (VRSP) Fellowship award, and Nigerian Communications Commission under Contract Number NCC/R&D/UNN/014.

Data availability

The data that support the findings of this research work are available from the corresponding author upon reasonable request.

Declarations

Competing interests The authors declare that they have no conflict of interest.

Supplementary Information The online version contains supplementary material available at https://doi.org/10.1007/s10854-023-11373-y.

References

1. M. Wu, S. Chan, M. Jao, W. Su, Sol. Energy Mater. Sol. Cells **157**, 447 (2016)
2. Q. Wali, F.J. Iftikhar, M.E. Khan, A. Ullah, Y. Iqbal, R. Jose, Org. Electron. **78**, 105590 (2020)
3. A. Kojima, K. Teshima, Y. Shirai, T. Miyasaka, J. Am. Chem. Soc. **131**, 6050–6051 (2009)
4. W.S. Yang, B.W. Park, E.H. Jung, N.J. Jeon, Y.C. Kim, D.U. Lee, S.S. Shin, J. Seo, E.K. Kim, J.H. Noh, S.I. Seok, Science **356**, 1376 (2017)
5. P. Zhang, M. Li, W.C. Chen, Front. Chem. **10**, 1 (2022)
6. M.A. Green, A. Ho-Baillie, H.J. Snaith, Nat. Photonics **8**, 506 (2014)
7. Z. Li, C.C. Mercado, M. Yang, E. Palay, K. Zhu, Chem. Commun. **53**, 2467–2470 (2017)

8. M.M. Lee, J. Teuscher, T. Miyasaka, T.N. Murakami, H.J. Snaith, Science **338**, 643–647 (2012)
9. H.S. Kim, C.R. Lee, J.H. Im, K.B. Lee, T. Moehl, A. Marchioro, S.J. Moon, R. Humphry-Baker, J.H. Yum, J.E. Moser, M. Grätzel, N.G. Park, Sci. Rep. **2**, 1 (2012)
10. C. Liang, P. Li, Y. Zhang, H. Gu, Q. Cai, X. Liu, J. Wang, H. Wen, G. Shao, J. Power Sources **372**, 235 (2017)
11. N.J. Jeon, J.H. Noh, Y.C. Kim, W.S. Yang, S. Ryu, S.I. Seok, Nat. Mater. **13**, 897 (2014)
12. G. Adam, M. Kaltenbrunner, E. Daniel, Sol. Energy Mater. Sol. Cell **157**, 318–325 (2016)
13. C. Chen, C. Li, F. Li, F. Wu, F. Tan, Y. Zhai, W. Zhang, Nanoscale Res. Lett. **9**, 457 (2014)
14. M. Ebrahimi, A. Kermanpur, M. Atapour, S. Adhami, R. Haji, E. Khorshidi, N. Irannejad, B. Rezaie, Sol. Energy Mater. Sol. Cells **208**, 110407 (2020)
15. Y. Tu, J. Wu, X. He, P. Guo, T. Wu, H. Luo, Q. Liu, K. Wang, J. Lin, M. Huang, Y. Huang, Z. Lan, S. Li, J. Mater. Chem. A **5**, 4376–4383 (2017)
16. P. Würfel, *Physics of solar cells: from principles to new concepts* (Wiley, Weinheim, 2005), pp.20–50
17. Y. Yamada, T. Nakamura, M. Endo, A. Wakamiya, Y. Kanemitsu, J. Am. Chem. Soc. **136**, 11610 (2014)
18. N. Marinova, W. Tress, R. Humphry-Baker, M.I. Dar, V. Bojinov, S.M. Zakeeruddin, M.K. Nazeeruddin, M. Grätzel, ACS Nano **9**(4), 4200–4209 (2015)
19. A. Fakharuddin, L. Schmidt-mende, G. Garcia-belmonte, R. Jose, I. Mora-sero, Adv. Energy Mater. **7**(22), 1700623 (2017)
20. A. Ruffo, M.C. Mozzati, B. Albini, P. Galinetto, M. Bini, J. Mater. Sci. Mater. Electron. **31**, 18263 (2020)
21. Z.L. Zhang, J.F. Li, X.L. Wang, J.Q. Qin, W.J. Shi, Y.F. Liu, H.P. Gao, Y.L. Mao, Nanoscale Res. Lett. **12**, 43–49 (2017)
22. M.F. Hossain, S. Naka, H. Okada, J. Photochem. Photobiol. A Chem. **360**, 109–116 (2018)
23. X.X. Gao, Q.Q. Ge, D.J. Xue, J. Ding, J.Y. Ma, Y.X. Chen, B. Zhang, Y. Feng, L.J. Wan, J.S. Hu, Nanoscale **8**, 16881–16885 (2016)
24. A.I. Rafieh, P. Ekanayake, A. Wakamiya, H. Nakajima, C.M. Lim, Sol. Energy **177**, 374 (2019)
25. P.S. Archana, R. Jose, M.M. Yusoff, S. Ramakrishna, P.S. Archana, R. Jose, M.M. Yusoff, S. Ramakrishna, Appl. Phys. Lett. **98**(15), 152106 (2011)
26. P.S. Archana, R. Jose, T.M. Jin, C. Vijila, M.M. Yusoff, S. Ramakrishna, J. Am. Ceram. Soc. **93**(12), 4096–4102 (2010)
27. Y. Lv, Y. Li, H. Sun, Y. Guo, Y. Li, J. Tan, X. Zhou, Thin Solid Films **651**, 117 (2018)
28. F. Giordano, A. Abate, J.P. Correa Baena, M. Saliba, T. Matsui, S.H. Im, S.M. Zakeeruddin, M.K. Nazeeruddin, A. Hagfeldt, M. Graetzel, Nat. Commun. **7**, 10379 (2016)
29. B. Mulyanti, C. Wulandari, L. Hasanah, R.E. Pawinanto, I. Hamidah, Model. Simul. Eng. (2022). https://doi.org/10.1155/2022/9299279
30. T.M.H. Nguyen, C.W. Bark, ACS Omega **5**(5), 2280–2286 (2020)
31. Y. Lv, B. Cai, Q. Ma, Z. Wang, J. Liu, W.H. Zhang, RSC Adv. **8**, 20982 (2018)
32. S. Wang, B. Liu, Y. Zhu, Z. Ma, B. Liu, X. Miao, R. Ma, C. Wang, Sol. Energy **169**, 335 (2018)
33. P.S. Archana, E.N. Kumar, C. Vijila, S. Ramakrishna, M.M. Yusoff, R. Jose, Dalton Trans. **42**(4), 1024–1032 (2013)
34. U. Nwankwo, S. Ngqoloda, A.C. Nkele, C.J. Arendse, K.I. Ozoemena, A.B.C. Ekwealor, R. Jose, M. Maaza, F.I. Ezema, RSC Adv. **10**, 13139 (2020)
35. P. Scherrer, Nachr. Ges Wiss Goettingen **26**, 98 (1918)
36. J.I. Langford, A.J.C. Wilson, J. Appl. Cryst. **11**, 102 (1978)
37. D.A.H. Hanaor, G. Triani, C.C. Sorrell, Surf. Coat. Technol. **205**, 3658 (2011)
38. J. Tauc, Mater. Res. Bull. **5**, 721–729 (1970)
39. P.S. Archana, A. Gupta, M.M. Yusoff, R. Jose, Phys. Chem. Chem. Phys. **16**, 7448–7454 (2014)
40. P. Docampo, J.M. Ball, M. Darwich, G.E. Eperon, H.J. Snaith, Nat. Commun. **4**, 1 (2013)
41. T. Hakamata, K. Shimamura, F. Shimojo, R.K. Kalia, A. Nakano, P. Vashishta, Sci. Rep. **6**, 1 (2016)
42. Y. Li, G. Zheng, J. Lin, Eur. J. Inorg. Chem. **4**, 1689 (2008)
43. X. Wang, Y. Fang, L. He, Q. Wang, T. Wu, Mater. Sci. Semicond. Process **27**, 569 (2014)